

Article

Strategy for Fast Decision on Material System Suitability for Continuous Crystallization Inside a Slug Flow Crystallizer

Anne Cathrine Kufner ^{1,†} , Adrian Krummnow ^{2,3,†} , Andreas Danzer ² and Kerstin Wohlgemuth ^{1,*} 

¹ Department of Biochemical and Chemical Engineering, Laboratory of Plant and Process Design, TU Dortmund University, D-44227 Dortmund, Germany

² Department of Biochemical and Chemical Engineering, Laboratory of Thermodynamics, TU Dortmund University, D-44227 Dortmund, Germany

³ AbbVie Deutschland GmbH & Co. KG, Global Pharmaceutical R&D, Knollstraße, D-67061 Ludwigshafen am Rhein, Germany

* Correspondence: kerstin.wohlgemuth@tu-dortmund.de; Tel.: +49-(0)-231-755-3020

† These authors contributed equally to this work.

Abstract: There is an increasing focus on two-phase flow in micro- or mini-structured apparatuses for various manufacturing and measurement instrumentation applications, including the field of crystallization as a separation technique. The slug flow pattern offers salient features for producing high-quality products, since narrow residence time distribution of liquid and solid phases, intensified mixing and heat exchange, and an enhanced particle suspension are achieved despite laminar flow conditions. Due to its unique features, the slug flow crystallizer (SFC) represents a promising concept for small-scale continuous crystallization achieving high-quality active pharmaceutical ingredients (API). Therefore, a time-efficient strategy is presented in this study to enable crystallization of a desired solid product in the SFC as quickly as possible and without much experimental effort. This strategy includes pre-selection of the solvent/solvent mixture using heuristics, verifying the slug flow stability in the apparatus by considering the static contact angle and dynamic flow behavior, and modeling the temperature-dependent solubility in the supposed material system using perturbed-chain statistical associating fluid theory (PC-SAFT). This strategy was successfully verified for the amino acids L-alanine and L-arginine and the API paracetamol for binary and ternary systems and, thus, represents a general approach for using different material systems in the SFC.

Keywords: continuous crystallization; microfluidics; slug flow; contact angle; solid–liquid interaction; solubility modeling



Citation: Kufner, A.C.; Krummnow, A.; Danzer, A.; Wohlgemuth, K. Strategy for Fast Decision on Material System Suitability for Continuous Crystallization Inside a Slug Flow Crystallizer. *Micromachines* **2022**, *13*, 1795. <https://doi.org/10.3390/mi13101795>

Academic Editor: Pingan Zhu

Received: 30 September 2022

Accepted: 19 October 2022

Published: 21 October 2022

Publisher's Note: MDPI stays neutral with regard to jurisdictional claims in published maps and institutional affiliations.



Copyright: © 2022 by the authors. Licensee MDPI, Basel, Switzerland. This article is an open access article distributed under the terms and conditions of the Creative Commons Attribution (CC BY) license (<https://creativecommons.org/licenses/by/4.0/>).

1. Introduction

In recent years, there has been increased research in the area of two-phase flow combined with micro- or minifluidics for a variety of application areas, such as measurement devices in life science and chemistry, as medical devices, microreactors, and heat exchangers, to name a few [1]. A further field of interest is crystallization as isolation technology for the small-scale production of active pharmaceutical ingredients (APIs). A typical production quantity for API production lies in the range of 250–1000 kg a^{−1}. Compared to other separation techniques, crystallization processes offer some key benefits, such as adjustable particular product properties and high product purity [2]. Therefore, one or even more crystallization steps are used in more than 90% of API production pathways [3]. The main specifications of the final product are a uniform particle size and shape to ensure constant bioavailability and dosage uniformity [4,5]. Operating modes for crystallization are batch, semi-batch, and continuous. The first mentioned are the most common ones in pharmaceutical crystallization due to the simplicity of apparatuses [4]. However, batch operation has some characteristic drawbacks, such as variability in product quality between batches, encrustation, and high capital costs [5,6]. Therefore, continuous crystallization

is advantageous due to high process reproducibility and uniform product quality while operating in a steady state. Furthermore, the higher process efficiency in terms of used substrates, and the use of the same equipment for research and design, as well as for industrial production by the extend of operating time, make the application highly attractive.

A distinction is made between two types of continuous crystallizers for the small-scale production range: mixed-suspension mixed-product removal (MSMPR) crystallizers and tubular plug-flow crystallizers (PFC) [7–9]. This work exploits the advantages of a special PFC, the slug flow crystallizer (SFC). The SFC is characterized by a gentle particle treatment with respect to particle suspension and a narrow residence time distribution (RTD) of the liquid and solid phases—basic prerequisites for obtaining a narrow particle size distribution (PSD) and high purity in a reproducible manner during crystallization. In the SFC, managing two immiscible fluids creates a slug flow pattern. Due to easier handling in further downstream and to avoid cross-contamination, gas–liquid segmentation is used in this study. Because of the wall friction, Taylor vortices are induced inside the liquid segments (slugs), which provide increased mixing of the liquid and suspension of particles. Accordingly, crystallization phenomena such as secondary nucleation or agglomeration are reduced.

However, the characteristics and advantages mentioned here only apply if a stable and uniform slug flow is achieved, which depends on many parameters: First, the choice of inner diameter for the tubing is decisive in order to force dominant surface effects and allow the simplified formation of slugs over the entire diameter [10,11]. Therefore, several criteria are postulated for the transition from macro- to mini- and microchannel, but there is no clear definition. Often, the Eötvös number $E\ddot{o}$ ($E\ddot{o} < 3.368$ [12], $E\ddot{o} < 0.88$ [13], $E\ddot{o} < (2 \cdot \pi)^2$ [14]) or the hydraulic diameter d_h [15–18] are used for confinement into the microscale range.

Second, the consideration of tubing material and material system (solute and solvent) combination is crucial. The property that receives special focus for the configuration of the slug shape is the three-phase contact angle Θ . It provides information on which of the two phases (gas or liquid) the wall-wetting phase is and whether convex or concave slugs are formed. Obtaining convex slugs is desirable in the case of crystallization since the RTD of the liquid phase corresponds to the RTD of the solid phase (particles) present in the liquid. This was demonstrated in our previous publication for crystallizing L-alanine from aqueous solution by using fluorinated ethylene propylene (FEP) as tubing material [19]. For aqueous systems, the utilization of a hydrophobic tubing material, such as FEP, leads to the avoidance of a wall film and the formation of convex slugs in the gas–liquid flow [20,21], whereas hydrophilic tubing material favors the undesirable wall crystallization [20]. In the literature, besides FEP [22–24], mostly silicone [20,21,25–29] or polyvinyl chloride (PVC) [20] are used as the tubing material for continuous crystallization applications. A wall film leads to broad RTDs if a material system is combined with a tubing material, where concave slugs are formed (rounded gas bubbles). Since gas bubbles roll over particles at the bottom, particles can be exchanged between neighboring slugs. Particles smaller than or equal to the wall film thickness are especially affected [29]. Accordingly, concave slugs lead to deviations between the RTDs of liquid and particles and negate the advantage of absent axial dispersion. Higher flow velocities increase this effect [29].

Consequently, it is necessary to consider gas–liquid interfacial tension $\sigma_{G/L}$, but also the solid–liquid ($\sigma_{S/L}$) and solid–gas ($\sigma_{S/G}$) interfacial tension. This relationship is described by Θ , which Young [30] defined (Equation (1)).

$$\sigma_{G/L} \cdot \cos(\Theta) = \sigma_{S/G} - \sigma_{S/L} \quad (1)$$

In the following, Θ serves as a parameter for the suitability of a material system for use in the crystallization process. Based on the literature on two-phase flow and the dependence of Θ on the tubing material and material system used [31–33], the wettability is divided into the intervals of highly wetting ($\Theta < 50^\circ$), marginally wetting ($50 < \Theta < 90^\circ$), and poorly wetting ($\Theta > 90^\circ$). A distinction is also made between wet and dry flow patterns [31,34]. The dry flow pattern describes the absence of the wall film and is desirable for crystallization

operation, but it also has the disadvantage that the pressure loss is higher due to the higher contact of the liquid with the wall in the apparatus. The dry pattern is not linked to a contact angle range, but its occurrence can be estimated using the capillary number Ca (Equation (2)), which implies that for $Ca < 10^{-3}$ (under flow boiling situations) [34–36] or, respectively, $Ca < 10^{-2}$ [37], dry plug flow occurs. Ca is determined by the ratio of flow velocity u and dynamic viscosity η with respect to the gas–liquid interfacial tension $\sigma_{G/L}$.

$$Ca = \frac{u \cdot \eta}{\sigma_{G/L}} \quad (2)$$

In general, particularly in further literature dealing with slug flow crystallization, Θ is given based on static contact angle (Θ_{stat}) measurements. However, a dynamic equilibrium is established in the apparatus so that the dynamic contact angle (Θ_{dyn}) may deviate from Θ_{stat} under certain conditions. For Θ_{dyn} , a distinction is made between a receding (at the front of a liquid slug) and an advanced (at the back of the liquid slug) contact angle. If these differ, this is referred to as contact angle hysteresis (CAH). The higher the hysteresis, the higher the probability of an unstable slug flow. This can be forced by surface disturbances or hydrodynamics, for example. Therefore, not only the Θ_{stat} is decisive for obtaining a stable slug flow and for the shapes of slugs, but also the CAH generated in the apparatus itself. Theoretically, by measuring the Θ of the slugs moving in the microchannel, it may be possible to correlate Θ_{dyn} as a function of the fluid velocities, as well as the material properties, and use this model to select the favored combination of the material system and tubing material in the SFC. Due to the difficulties in measuring Θ_{dyn} on such a small scale, as well as the complexity of the multiphase flow, other methods are preferred. Therefore, Θ_{stat} measurements are used in most cases to approximate the dynamic behavior. For instance, in a rectangular tubing for the range of capillary number Ca from 10^{-6} to 10^{-4} , Skartsis et al. [38] have shown that the dynamic contact angle can be well approximated by the static one. However, this conclusion cannot be directly transferred to all tubing geometries, material systems, and operating conditions. Therefore, Θ_{stat} and Θ_{dyn} should be checked qualitatively for a new material system.

In combination with crystallization, the choice of a new material system poses a number of additional challenges for operation in the SFC, besides the requirements for slug flow stability, since a high product quality in terms of mean particle size and width of PSD is aimed for, but also a high yield should be maintained. Therefore, besides demands for process safety, which include toxicity, explosion-proof environment, and more, the component's solubility in the solvent and its temperature dependency are crucial. If the solute solubility in the solvent is very low, the amount of solvent required is very high, and the mass of solids per volume of solvent is minimal. Furthermore, for the application in cooling crystallization, the temperature dependency of solubility is of decisive importance. In addition to other criteria, such as the lowest possible toxicity and chemical stability of the solute in the considered application range, the solvent's viscosity should be low for good mass and heat transfer.

In conclusion, selecting a new and suitable material system for crystallization in the SFC is challenging and linked to many constraints to maintain slug flow stability and consequently obtain high product quality at the end of the apparatus. Therefore, this work aims to present a systematic approach to decide material system suitability as fast as possible and with low experimental effort in order to enable the continuous operation of the desired product using cooling crystallization inside the SFC. This structured procedure includes the selection of a suitable solvent for the desired solid via a screening of different solvents and tubing materials and the evaluation of the suitability for the SFC reviewing Θ_{stat} . Furthermore, the suitability of the selected solvent/tubing material combination is validated by examining the dynamic behavior in the apparatus with regard to flow stability. As the last step, the temperature-dependent solute's solubility in the solvent is modeled and predicted to evaluate the possible yield for crystallization processes. With the help of

this strategy, it is possible to ensure the crystallization of a new material system in the SFC within four steps for binary and ternary systems.

- (1) Pre-selection of solvents for the crystallization of the desired solid compound
- (2) Static contact angle measurements
- (3) Proof of slug flow stability inside the apparatus
- (4) Solubility modeling

2. Substances Used

Several common solvents were considered to select an appropriate solvent for crystallization inside the SFC by Θ_{stat} measurements. This involves the use of ultrapure, deionized, and bacteria-free filtered water (Milli-Q[®], $\sigma_{\text{G/L}}$ (298.15 K) = 72.04 mN m⁻¹ [39]) with a total organic carbon content of maximal 3 ppb, purified by a Milli-Q[®] Advantage A10 apparatus of Merck KGaA. As one product component, L-alanine (Ala) purchased by Evonik Industries AG with a purity of 99.7% was selected as it has similar particulate properties as high-priced APIs. The saturated aqueous solution was set according to the measurements and regressed data of Wohlgemuth et al. [40] (Equation (3)).

$$c^* \left(g_{\text{Ala}} g_{\text{solution}}^{-1} \right) = 0.11238 \cdot \exp \left(9.0849 \cdot 10^{-3} \cdot \vartheta^* (\text{°C}) \right) \quad (3)$$

As a further solid compound, L-arginine (Arg, purity > 99%, Merck KGaA) was chosen in order to prove the concept transferability with another amino acid. The following solubility equation was used (Equation (4)) to prepare a saturated aqueous solution and is based on gravimetric measurements conducted in this work.

$$c^* \left(g_{\text{Arg}} g_{\text{solution}}^{-1} \right) = 0.089 \cdot \exp \left(2.57 \cdot 10^{-2} \cdot \vartheta^* (\text{°C}) \right) \quad (4)$$

Since the water solubility of APIs is usually low, leading to limited bioavailability [41], paracetamol (APAP, acetaminophen according to USP, > 99%, Merck KGaA) was used as a third solid compound to demonstrate the application field of APIs. The regression curve of the saturated aqueous solution was calculated and used according to the measured data from Grant et al. [42] given in Equation (5).

$$c^* \left(g_{\text{APAP}} g_{\text{solution}}^{-1} \right) = 0.0067 \cdot \exp \left(3.18 \cdot 10^{-2} \cdot \vartheta^* (\text{°C}) \right) \quad (5)$$

Further solvents studied were ethanol absolute (99.9%, VWR, $\sigma_{\text{G/L}}$ (298.15 K) = 21.72 mN m⁻¹ [39]), 2-propanol (99.9%, VWR, $\sigma_{\text{G/L}}$ (298.15 K) = 21.74 mN m⁻¹ [43]), acetone ($\geq 99.5\%$, Roth, $\sigma_{\text{G/L}}$ (298.15 K) = 22.57 mN m⁻¹ [44]) and n-hexane (95%, VWR, $\sigma_{\text{G/L}}$ (298.15 K) = 17.78 mN m⁻¹ [45]). These (along with water) five solvents are considered first because they are common solvents used for other separation technologies such as extraction processes and are often upstream of crystallization processes [46].

Requirements for tubing material selection are thermal and chemical resistance to a broad spectrum of solvents. For analytical reasons, the transparency of the tubing would be advantageous but not mandatory. Besides FEP, which was successfully used in our previous publications [19,47,48], other materials such as aluminum, glass, polystyrene, and silicone were also tested via the Θ_{stat} measurements for their suitability as a tubing material for the SFC.

Synthetic air (Grade 5.0, Messer Griesheim) was utilized as second fluid phase to generate slug flow inside the tubing.

3. Modeling of Solubilities Using PC-SAFT Equation of State

According to the presented strategy, the modeling of the solubility within the system under consideration is carried out after selecting the solvent based on Θ_{stat} measurements.

The mole fraction solubility x_i^L of component i in a solvent (or solvent mixture) was determined by considering an equilibrium between a pure solid phase and a liquid phase according to Prausnitz (Equation (6)) [49]:

$$x_i^L = \frac{1}{\gamma_i^L} \exp \left[\frac{\Delta h_i^{SL}}{RT_i^{SL}} \left(1 - \frac{T_i^{SL}}{T} \right) - \frac{1}{RT} \int_{T_i^{SL}}^T \Delta c_{p,i}^{SL}(T) dT + \frac{1}{R} \int_{T_i^{SL}}^T \frac{\Delta c_{p,i}^{SL}(T)}{T} dT \right] \quad (6)$$

R is the universal gas constant, T is the system temperature, T_i^{SL} is the melting temperature of component i , and Δh_i^{SL} is the melting enthalpy at the melting temperature of component i . For amino acids, the difference between the component’s liquid and solid heat capacity $\Delta c_{p,i}^{SL}$ was recently assumed to be linear dependent on temperature (Equation (7)) [50]:

$$\Delta c_{p,i}^{SL}(T) = \Delta a_{c_{p,i}^{SL}} T + \Delta b_{c_{p,i}^{SL}} \quad (7)$$

The combination of a slope $\Delta a_{c_{p,i}^{SL}}$ and an intercept $\Delta b_{c_{p,i}^{SL}}$ was used for Ala and Arg in this work. For active pharmaceutical ingredients, such as APAP, the difference between the component’s liquid and solid heat capacity is often assumed to be insensitive to temperature [51]. Thus, APAP was modeled with the heat capacity difference at the melting temperature in this work. All melting properties were taken from the literature and are listed in Table 1.

Table 1. Pure-component melting properties of Ala, APAP, and Arg at 0.1 MPa.

Component	T_i^{SL}/K	$\Delta h_i^{SL}/kJ \text{ mol}^{-1}$	$\Delta a_{c_{p,i}^{SL}}/J \text{ mol}^{-1} \text{ K}^{-2}$	$\Delta b_{c_{p,i}^{SL}}/J \text{ mol}^{-1} \text{ K}^{-1}$
Ala	608.0 [52]	25.99 [50]	−0.057 [50]	39.923 [50]
Arg	558.0 [50]	32.00 [50]	−0.364 [50]	237.991 [50]
APAP	443.6 [53]	27.10 [53]	0 ¹	99.800 [54]

¹ Assumption of $\Delta c_{p,i}^{SL}(T) = \Delta c_{p,i}^{SL}(T_i^{SL})$ in this work.

The activity coefficient γ_i^L of a component i accounts for deviation from ideal-mixture behavior in the liquid phase and is related to the partial derivatives of the residual Helmholtz energy with respect to the mole fraction. Within the perturbed-chain statistical associating fluid theory (PC-SAFT) equation of state, the residual Helmholtz energy a^{res} is expressed by the sum of a hard-chain (a^{hc}), dispersion (a^{disp}), and association (a^{assoc}) Helmholtz energy contribution (Equation (8)) [55]:

$$a^{\text{res}} = a^{\text{hc}} + a^{\text{disp}} + a^{\text{assoc}} \quad (8)$$

These contributions account for repulsion, van der Waals attractions, and hydrogen bonds. Calculation requires the segment number m_i^{seg} , the segment diameter σ_i , the dispersion energy parameter $u_i k_B^{-1}$, the association energy parameter $\epsilon^{A_i B_i} k_B^{-1}$, the association volume $\kappa^{A_i B_i}$, and the number of association sites N_i^{assoc} of every component i . k_B is the Boltzmann constant. The pure-component parameters used in this work were available in the literature and are summarized in Table 2.

Table 2. PC-SAFT pure-component parameters of Ala, Arg, APAP, water, and ethanol.

Component	$M_i/g \text{ mol}^{-1}$	$m_i^{\text{seg}} M_i^{-1}/\text{mol g}^{-1}$	$\sigma_i/\text{\AA}$	$u_i k_B^{-1}/K$	$\epsilon^{A_i B_i} k_B^{-1}/K$	$\kappa^{A_i B_i}$	N_i^{assoc}
Ala [56]	89.090	0.0613	2.5222	287.590	3176.600	0.0819	1/1
Arg [56]	174.210	0.0569	2.6572	349.710	2555.450	0.0393	3/1
APAP [57]	151.160	0.0498	3.5080	398.284	1994.200	0.0100	2/2
Water [58]	18.015	0.0669	σ_{water}^*	353.950	2425.700	0.0451	1/1
Ethanol [55]	46.069	0.0517	3.1770	198.237	2653.384	0.0320	1/1

* $\sigma_{\text{water}} = 2.7927 + 10.11 \exp(-0.01755 T/K) - 1.417 \exp(-0.01146 T/K)$.

To calculate the segment diameter and the dispersion energy in mixtures of components i and j the combining rules as suggested by Berthelot [59] and Lorentz [60] were used:

$$\sigma_{ij} = \frac{1}{2}(\sigma_i + \sigma_j) \tag{9}$$

$$u_{ij} = \sqrt{u_i u_j}(1 - k_{ij}) \tag{10}$$

The binary interaction parameter k_{ij} was introduced for correction of deviations from the geometric mean of the dispersion energies of the pure components and is usually fitted to experimental data of binary mixtures. A linear temperature dependency was assumed in this work:

$$k_{ij} = k_{ij,m}T + k_{ij,b} \tag{11}$$

The slope $k_{ij,m}$ and intercept $k_{ij,b}$ for Ala/water, Arg/water, APAP/water, and water/ethanol were taken from the literature and are given in Table 3. The interaction parameters for Ala/ethanol, APAP/ethanol, and Arg/ethanol were fitted to solubility data from An et al. [61], this work, and Jiménez and Martínez [62], respectively, and are also available in Table 3.

Table 3. PC-SAFT interaction parameters for mixtures of Ala, Arg, APAP, water, and ethanol.

Mixture	$k_{ij,m}/\text{K}^{-1}$	$k_{ij,b}$
Ala/water [56]	2.910×10^{-4}	-0.147962
Ala/ethanol ¹	1.140×10^{-3}	-0.3513
Arg/water [56]	0	-0.0145
Arg/ethanol ²	2.075×10^{-4}	-0.134529
APAP/water [63]	1.770×10^{-4}	-0.051
APAP/ethanol ³	1.250×10^{-4}	-0.08764
water/ethanol [64]	6.860×10^{-4}	-0.2662

¹ Fitted to solubility data of An et al. [61] in this work. ² Fitted to solubility data from this work. ³ Fitted to solubility data of Jiménez and Martínez [62] in this work.

The association energy and association volume in mixtures of components i and j were determined by applying the combining rules of Wolbach and Sandler [65]:

$$\epsilon^{A_i B_j} = \frac{1}{2}(\epsilon^{A_i B_i} + \epsilon^{A_j B_j}) \tag{12}$$

$$\kappa^{A_i B_j} = \sqrt{\kappa^{A_i B_i} \kappa^{A_j B_j}} \left(\frac{\sqrt{\sigma_i \sigma_j}}{\frac{1}{2}(\sigma_i + \sigma_j)} \right)^3 \tag{13}$$

4. Strategy for Solvent Selection

In order to limit the solvent selection for a specific solid product, in this case Ala, Arg, and APAP, it is important to ensure stable slug flow inside the crystallizer. Furthermore, since the objective is to obtain a high product quality in terms of purity and maintain a narrow PSD, for the latter it is necessary to prevent a wall film (i.e., realize dry plug flow) and, thus, facilitate convex slugs. Therefore, the static contact angle is used in order to select appropriate solvents for crystallization in this apparatus. Afterwards, the dynamic behavior and slug flow stability are proved and correlated to the capillary number Ca . Subsequently, the solubility modeling of the selected material system is carried out, which completes the requirements for successful crystallization in the apparatus.

4.1. Static Contact Angle Measurements

The Θ_{stat} between solid wall material, liquid, and gaseous phase is crucial for these applications. Therefore, Θ_{stat} measurements were carried out with a drop shape analyzer (DSA30, Krüss) equipped with a DS4210 dosing unit and the software ADVANCED to provide initial estimates of the suitability of solvents for SFC application. The measurements are based on the sessile drop method, where a droplet is placed onto the solid surface to be examined by a cannula ($d_i = 0.75$ mm). In each case, ten measurements of Θ at the right and left edge of the droplet are measured for three drops (3–20 μL) of a solvent/mixture, and the average value is calculated.

Results of Static Contact Angle Measurements

The results of Θ_{stat} measurements of solvents on different tubing materials are presented in Table 4.

Table 4. The measured Θ_{stat} for different tubing materials and solvent combinations.

	$\Theta_{\text{stat}}/^\circ$ Glass	$\Theta_{\text{stat}}/^\circ$ Aluminum	$\Theta_{\text{stat}}/^\circ$ Polystyrene	$\Theta_{\text{stat}}/^\circ$ Silicone	$\Theta_{\text{stat}}/^\circ$ FEP
n-Hexane	<20	<20	<20	<20	<20
Isopropanol	<20	<20	<20	<20	36.65 ± 1.37
Acetone	<20	<20	<20	<20	47.33 ± 3.48
Ethanol	<20	<20	<20	23.10 ± 1.34	45.51 ± 3.68
Water	20.89 ± 1.09	66.44 ± 1.41	81.98 ± 0.43	97.99 ± 0.38	100.66 ± 1.37

Values $< 20^\circ$ indicate that a measurement of a droplet via the software was not possible, caused by the low Θ_{stat} . Therefore, the combination of solvent, solid material, and air was assumed to be completely wetted and unsuitable for the use inside the SFC. Using a non-polar solvent (n-hexane) leads to complete wetting of all tested wall materials; hence, n-hexane is not a suitable solvent for SFC. Comparing the surface tensions of ethanol, acetone, and isopropanol (see Section 2), they are in a similar range, and, therefore, the Θ_{stat} are also in a similar range, despite their different solvent nature of polar protic and polar aprotic. However, since Θ_{stat} of isopropanol, acetone, and ethanol are $< 50^\circ$ with all materials tested, they are also classified as highly wetting and, thus, not suitable for SFC crystallization. It is becoming clear that water forms higher Θ_{stat} with all the materials tested than the other solvents due to its high $\sigma_{\text{G/L}}$. It also can be seen that the most hydrophobic wall material tested, FEP, forms higher Θ_{stat} compared to the other materials. Therefore, the following focuses on FEP as a wall material.

Figure 1 shows the Θ_{stat} of solvent/FEP combinations, which are listed in Table 4. According to the literature, a poorly wetting system ($\Theta > 90^\circ$) is preferred. Consequently, combining an aqueous system and FEP as tubing material is the most suitable setup for crystallization purposes inside SFC for the tested combinations since $\Theta_{\text{stat}} > 100^\circ$. This indicates that convex slugs are formed, and the presence of a wall film is negligible.

Conversely, solvents that form a $\Theta_{\text{stat}} < 90^\circ$ with FEP as the wall material do not appear suitable for use in the SFC. This correlation based on Θ_{stat} measurements is further verified in the next section by reviewing the transport of slugs of all tested solvents in an FEP tubing in order to evaluate the corresponding dynamic behavior.

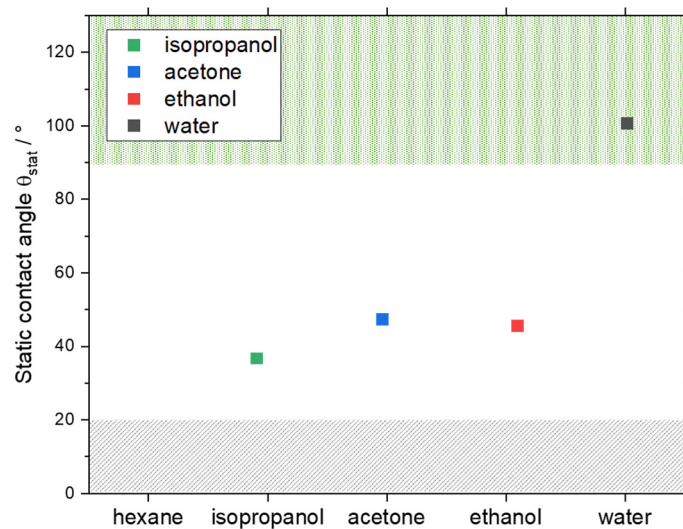


Figure 1. θ_{stat} for the respective solvents is shown. The grey marked area indicates the region in which θ_{stat} measurements were not possible ($\theta_{\text{stat}} < 20^\circ$) with the method described before in Section 4.1. The green area ($\theta_{\text{stat}} \geq 90^\circ$) marks the θ_{stat} at which a non-wetting behavior is expected, and a stable slug flow might be generated.

4.2. Proof of Stable Slug Flow Inside SFC

In the following, in order to connect the results from θ_{stat} measurements and the solubility modeling with the operation inside the SFC and proof of the suitability of the solvent for crystallization purposes, the setup as schematically shown in Figure 2 was applied. The setup can be divided into slug formation and slug flow zone, including image analysis. A solvent, solvent mixture, or saturated solution, which applicability has to be checked, is given inside a feed vessel. For the case of using a saturated solution, those were prepared by setting up a slightly supersaturated solution according to Equation (3), Equation (4), or Equation (5), followed by stirring for 48 h and filtering. The liquid is pumped via a peristaltic pump (*Ismatec Reglo Digital MS-4/12*, $d_i = 2.29$ mm Pharmed) to the slug formation zone. This consists of a T-junction (polypropylene, PP) in which the feed is fed from one side and synthetic air supplied via pipeline pressure from a gas cylinder from the other, forming alternating gas and liquid segments of equal size, respectively. The gaseous volume flow rate was controlled by a high-resolution needle valve (NV-001-HR, *Bronkhorst*) and a flow meter (El-Flow-Select, *Bronkhorst*). The choice of a T-junction is critical for the slug length distribution and its reproducibility throughout the slug flow zone since a squeezing mechanism is evoked as slug formation mechanism, which has already been demonstrated in our previous publication [47]. The inner diameter of the T-junction was chosen to $d_i = 3$ mm similar to the tubing's inner diameter ($d_{i,\text{tubing}} = 3.18$ mm) to minimize the slug length variability [66]. After the slug flow was built, the slugs were transported through the FEP tubing ($L_{\text{tubing}} = 7.5$ m, $d_{\text{out,tubing}} = 4.76$ mm) in the slug flow zone covered with a polyvinyl chloride (PVC) cooling jacket ($d_i = 15$ mm), which is filled with deionized water. As no cooling crystallization experiment was performed in this study, no cooling profile was adjusted, and the experiments were conducted at ambient temperature ($\vartheta_{\text{amb}} \approx 22$ °C).

At the end of SFC tubing, a camera (*Samsung NX 300*, 18–55 mm lens) is placed in order to evaluate the slug shape and slug length distribution by image analysis. Therefore, the process tubing is placed in a glass box (14 cm × 6 cm × 6 cm) filled with degassed water at ambient temperature. The back of the box is darkened with black cardboard and a LED lamp (*LED Panel Light* from *LED Universum*) is placed above the box for indirect illumination. This procedure minimizes reflections and light influences from the environment and creates a high contrast for the evaluation of the resulting videos. The image evaluation is conducted by an in-house MATLAB script, which has already been described

in a previous publication [47]. The slug length and CAH are evaluated quantitatively and the slug shape qualitatively.

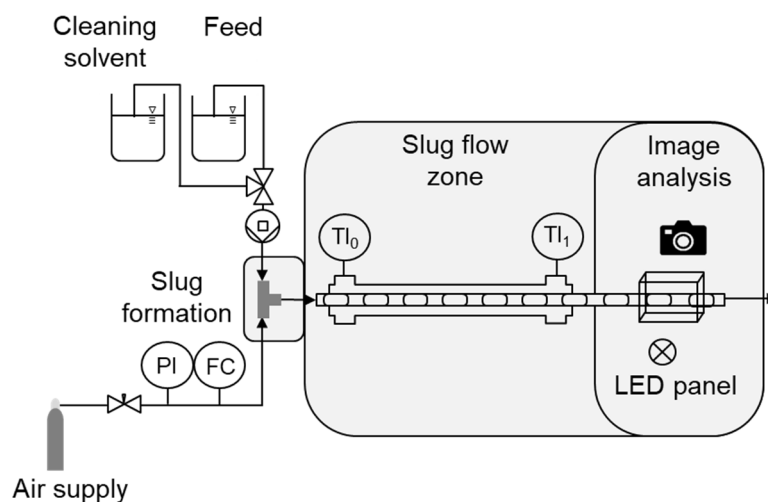


Figure 2. Schematic setup for the validation of solvent suitability for slug flow crystallization.

Results of Proof of Slug Flow Stability

Images of slugs during operation with different solvents at the end of the apparatus consisting of an FEP tubing are shown in Figure 3.

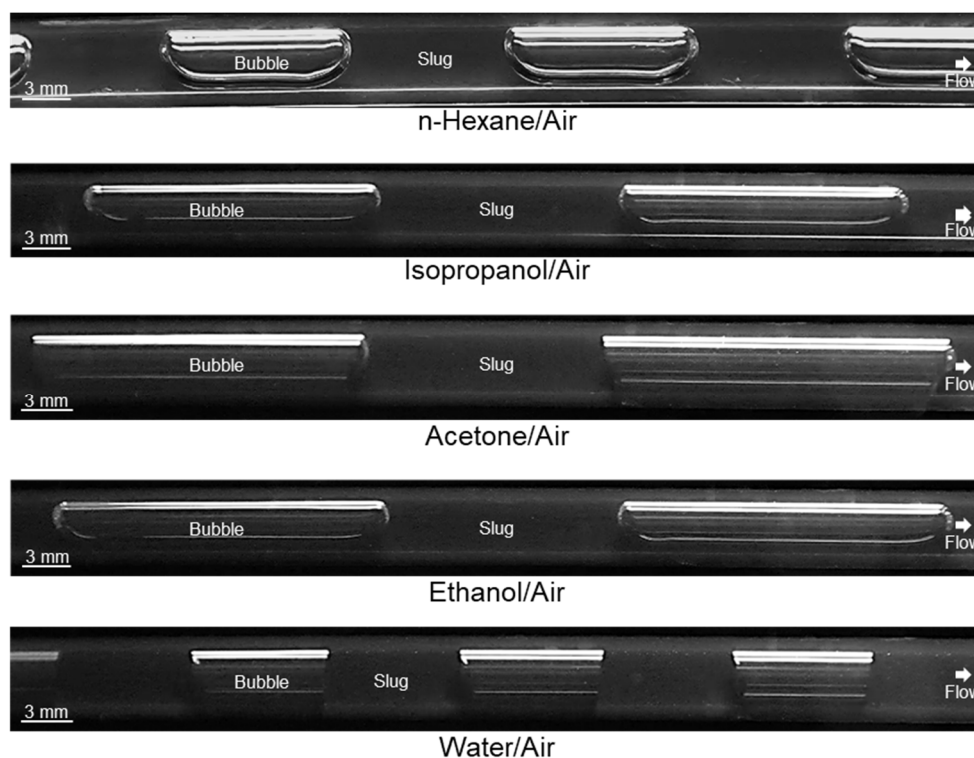


Figure 3. Images of slugs at the end of the apparatus ($L = 7.5$ m) during operation with different solvents in an FEP tubing. The liquid and gas flow rates were set to $Q = 10$ mL min^{-1} each. The experiments were conducted at ambient temperature ($\vartheta_{\text{amb}} \approx 22$ °C).

In all cases, the gas bubble extends over the entire diameter of the tubing, and stable slug flow is formed independently of the solvent used and its Θ_{stat} described in Table 4. Via image analysis, it was quantitatively demonstrated that for each solvent, slugs of equal size are formed, but differences in slug length occur depending on the solvent applied (Table 5). During experiments, it was observed that this is due to the changing slug mechanism in the slug formation zone. While in the case of n-hexane, isopropanol, acetone, and ethanol, the dripping mechanism was observed to form the slugs, in the case of water, the squeezing mechanism produces the slugs.

Table 5. Median slug length L_{50} and slug length distribution L_{90-10} at the end of the apparatus ($L_{\text{tubing}} = 7.5$ m) for the operation with different solvents. The experiments were conducted at ambient temperature ($\vartheta_{\text{amb}} \approx 22$ °C).

	L_{50}/mm	L_{90-10}/mm
n-Hexane	10.70	2.23
Isopropanol	24.30	1.27
Acetone	16.37	2.45
Ethanol	20.58	0.85
Water	10.16	0.99

The squeezing mechanism is desirable for the reproducibility of the slug length according to the literature [47,67,68] and the desired and set operating conditions of short slugs. In general, the slug length is relevant because it influences pressure drop, mixing, suspension of particles, and heat transfer [47,66,69]. The slug length is influenced by mixer geometry and dimension, mixer material/three-phase contact angle, phase ratio/liquid hold-up, velocity of the phases, properties of the phases, supplying of the phases, and the bubble detachment mechanism [47,70,71]. All these influences have to be considered when designing a new apparatus for a new material system.

However, not only slug length, but also slug shape is crucial for crystallization purposes. According to Figure 3, a significant difference in slug shape can be seen for the different solvents tested. While the gas bubbles are rounded in the case of n-hexane, ethanol, and isopropanol, clear edges can be seen in the case of water. For acetone, a transitional form is visible, showing less curvature of the bubble cap compared to the bubbles for n-hexane, ethanol, and isopropanol slugs. The rounded shape of the gas bubbles can lead to the fact that in the presence of crystals in the liquid phase, the crystals can migrate between neighboring slugs and, thus, significantly broaden the RTD of the solid phase. Based on the curvature of the gas bubbles, it can be seen that for the n-hexane, ethanol, and isopropanol slugs, a wall film is present, whereas the contact of the gas bubble and the wall is increased in the case of acetone and water. Therefore, the slug flow for acetone and water is visually assigned to the dry pattern, which is preferred for crystallization. This assignment is confirmed by considering the Ca number for the used solvents (Figure 4). The values for hexane, water, and acetone are higher than the values for ethanol and isopropanol ($Ca_{\text{EtOH}} = 2.3 \cdot 10^{-3}$; $Ca_{\text{IPA}} = 4.8 \cdot 10^{-3}$; $Ca_{\text{Ac}} = 5.9 \cdot 10^{-4}$; $Ca_{\text{wat}} = 5.8 \cdot 10^{-4}$; $Ca_{\text{hexane}} = 7.3 \cdot 10^{-4}$). Since all calculated Ca numbers are $< 10^{-2}$, the higher limit postulated in the literature [37] is not sufficient to predict the dry pattern in our case. The limit of $Ca < 10^{-3}$ [34] is applicable to our purposes in the meantime as hexane has already been excluded for suitability due to its non-polar properties.

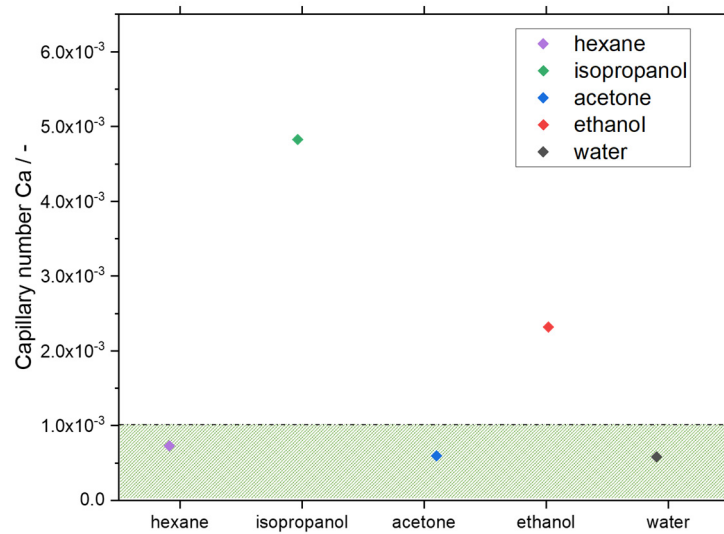


Figure 4. Calculated Ca numbers for the tested solvents in the SFC. The calculation was performed for the operating parameters based on the slug flow stability experiments at liquid and gas flow rates of $Q = 10 \text{ mL min}^{-1}$ each and a ambient temperature of $\theta_{amb} \approx 22 \text{ }^\circ\text{C}$. The green area marks the dry pattern slug flow range according to the limit of $Ca < 10^{-3}$.

Furthermore, it is recognizable that no constant Θ_{dyn} is formed in the apparatus itself, as in the case of Θ_{stat} , but different dynamic contact angles Θ_{dyn} are present depending on whether at the bottom or top of the slug, left or right. The sampled Θ_{dyn} from the experiment shown in Figure 3 indicates that the receding contact angle is smaller than the advanced contact angle for rounded bubbles, confirming the literature. In addition, the literature states that as Ca increases, the CAH range becomes broader [34]. The measured ranges of receding and advanced contact angles for the cases considered are shown in Table 6.

Table 6. Measured receding and advanced dynamic contact angle ranges for the different solvent used in the experiments. CAH_{max} is built by the lowest value for receding and highest advanced dynamic contact angle value for the respective solvent.

Solvent	$\Theta_{dyn}/^\circ$ Receding	$\Theta_{dyn}/^\circ$ Advanced	$CAH_{max}/^\circ$
n-Hexane	20–34	25–36	16
Isopropanol	36–63	47–64	28
Acetone	50–60	65–73	23
Ethanol	26–41	40–56	30
Water	82–92	84–92	10

Although the difference in receding and advanced Θ_{dyn} observed in the experiments differ significantly, no instability of the slug flow has been observed, so the critical CAH has not been exceeded. If the absolute values of the dynamic contact angles are considered, the static contact angles are near the range of the dynamic contact angles for water, ethanol, isopropanol, and hexane slugs. However, this does not apply to the acetone slugs. In this case, the static contact angle is lower than the dynamic ones. Due to the lower curvature of the gas bubble and correspondingly higher Θ_{dyn} , it is to be expected that the particles in the slugs can be better transported along. This shows that, in addition to the wetting properties, the hydrodynamics are also decisive and must be taken into account. Furthermore, solvents' volatility should be checked to avoid the expansion of the gas bubble and the change in slug form during the operation. Summarizing, the combination of estimating the Ca number and using the Θ_{stat} appears to be sufficient to have a first indication of the slug shape. A dry pattern is expected for $Ca < 10^{-3}$ and $\Theta_{stat} \geq 90^\circ$.

4.3. Proving the Operability of Slug Flow Crystallizer with the Solutes

As described in the introduction, some material systems have already been used for SFC crystallization, mainly amino acids or proteins. A previous publication has already demonstrated the evidence of convex slugs for a saturated Ala/water solution in the crystallization process [19]. The measured $\Theta_{\text{stat}} = 98.45^\circ \pm 1.69^\circ$ and calculated $Ca_{\text{AlaSolution}} = 6.3 \cdot 10^{-4}$ for the same operating conditions fulfills the above-mentioned criteria.

To verify the hypothesis to other solid compounds, another amino acid, Arg, which to our best knowledge has not yet been used in the literature for SFC, and APAP are chosen. The solvent selection has already been made in Section 4.1, so for the solutes Arg and APAP water seems ideal as a solvent in an FEP tubing with regard to the slug flow stability and slug shape. The solute influences the contact angle depending on the hydrophobicity of the amino acid side chain and the structure of the molecule [72,73]. The measured Θ_{stat} of the saturated aqueous solutions of both solutes on the FEP tubing material result in $\Theta_{\text{stat,Arg}} = 93.26 \pm 1.22^\circ$ and $\Theta_{\text{stat,APAP}} = 90.61 \pm 1.62^\circ$. Therefore, both solutes have higher impact on the Θ_{stat} than Ala but are still $>90^\circ$. The Ca numbers were calculated to $Ca_{\text{ArgSolution}} = 8.7 \cdot 10^{-4}$ for a saturated Arg/water solution and $Ca_{\text{APAPSolution}} = 6.3 \cdot 10^{-4}$ for the saturated APAP/water solution. Consequently, both solute/solvent combinations seem to be suitable for crystallization inside the SFC by fulfilling the criteria so that convex slugs should be formed. Evidence of slug shape and stable slug flow in the apparatus can be seen in Figure 5.

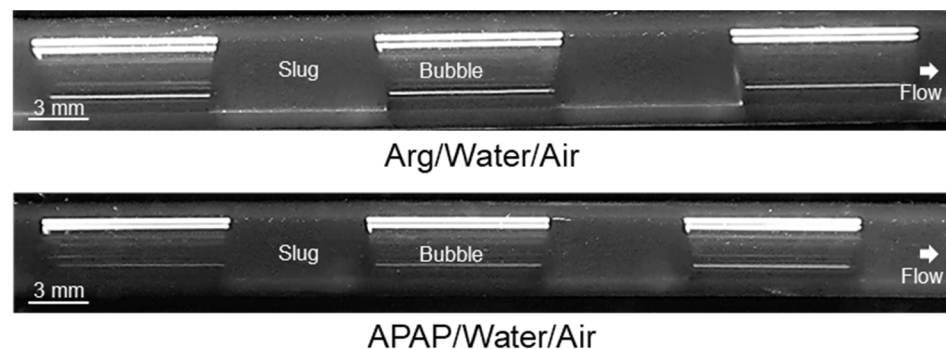


Figure 5. Images of saturated Arg/water (top) and APAP/water (bottom) slugs at the end of the apparatus ($L_{\text{tubing}} = 7.5$ m) during operation inside an FEP tubing of SFC. The liquid and gas flow rates were set to $Q = 10 \text{ mL min}^{-1}$ each. The experiments were conducted at ambient temperature ($\theta_{\text{amb}} \approx 22^\circ \text{C}$).

In both cases, stable slug flow was observed over the entire tubing length. The dry pattern, which was already anticipated by the Ca numbers, can be confirmed visually for both solutes. Furthermore, the slug shape is convex according to the heuristics, so no wall film is present, and a narrow RTD of liquid and solid phases could be achieved. For evaluation of slug flow stability and slug length reproducibility for the saturated Arg/water solution, the characteristic values of slug length distribution were calculated to $L_{50} = 10.04$ mm and $L_{90-10} = 0.59$ mm. For the saturated aqueous APAP solution, slug lengths of $L_{50} = 9.82$ mm and $L_{90-10} = 2.24$ mm were achieved. Based on the Θ_{stat} measurements and the verification of the dynamic behavior inside the SFC, the combination of the two solutes Arg and APAP, respectively, with water is suitable for crystallization in the apparatus and fulfills the requirements with respect to slug flow stability and slug shape for obtaining a high product quality. For further evaluation of the material systems with respect to the suitability for cooling crystallization, temperature-dependent solute solubilities are modeled for the three presented solutes as a next step.

4.4. Solubilities for Binary Systems

Figure 6 shows the modeled temperature-dependent solubilities of Ala, Arg, and APAP in water (a) and ethanol (b) at 0.1 MPa using PC-SAFT compared to experimental data. The solubility lines were modeled with the parameters from Tables 1–3. Modeling results and experimental data (from the literature, as well as from gravimetric measurements performed in this work) are in very good agreement. PC-SAFT reveals a high accuracy in predicting solubilities over a wide temperature range.

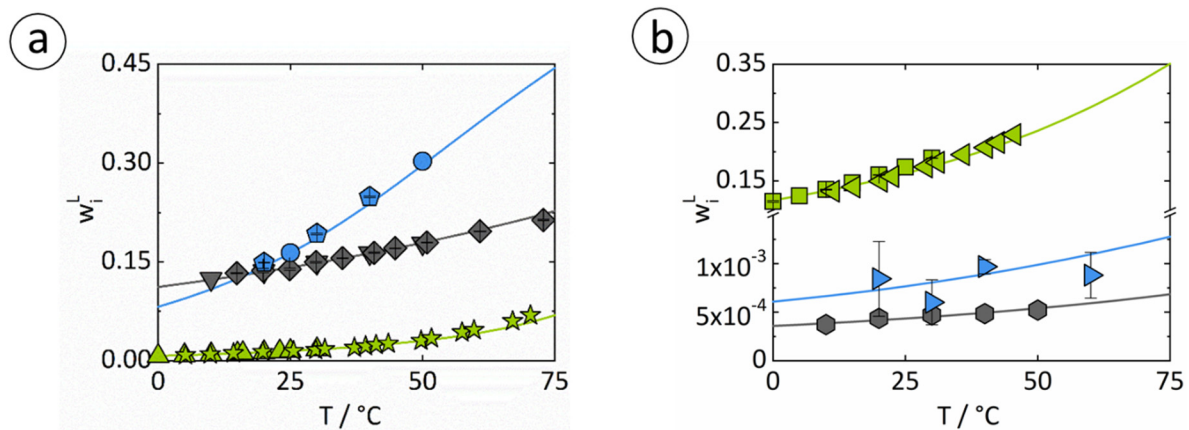


Figure 6. Solubilities of Ala (gray), Arg (blue), and APAP (green) in water (a) and ethanol (b) at 0.1 MPa: Down-pointing triangles, diamonds, circles, up-pointing triangles, and stars depict measured solubilities in water from An et al. [61], Grosse Daldrup et al. [74], Amend and Helgeson [75], Granberg et al. [76], and Grant et al. [42]. Hexagons, squares, and left-pointing triangles denote solubility measurements in ethanol from An et al. [61], Granberg et al. [53], and Matsuda et al. [77]. Pentagons and right-pointing triangles are measurements in water and in ethanol performed in this work, respectively. The solid lines are modeled solubility lines using PC-SAFT.

Above the solubility lines are the two-phase regions in which crystallization occurs if an initially homogeneous mixture is cooled starting below the solubility line across the solubility line. Arg solubilities in water are high, whereas the solubility line strongly depends on temperature. Thus, the Arg/water system is well suitable for cooling crystallization as it enables high yields. This is not the case for the other modeled systems. Ala solubilities in water are high, but the temperature dependence of the solubility line is much less pronounced, so yields are too low. In the APAP/water system, the solubilities are comparatively lower than in the other systems. Moreover, the temperature dependence is again too low to reach sufficient yields when applying cooling crystallization.

To increase the yield in the case of APAP/water for crystallization in the SFC, the application in the ternary system is possible. In order to solubilize, ethanol seems to be useful as an increase in yield due to the higher solubility of APAP in ethanol compared to water. Furthermore, ethanol is suitable as a wash liquid in the downstream processing of Ala [78] and can also serve as an antisolvent in the crystallization process of Ala and Arg in aqueous solutions.

5. Consideration of Ternary Systems for Slug Flow Crystallizer Application

In order to extend the possible field of application, the strategy shown above is applied to ethanol/water mixtures. Therefore, solubility modeling of Ala, Arg, and APAP in a ternary system is first performed to determine the influence of different compositions of ethanol/water on solute solubility. Afterwards, it is identified which fractions of ethanol in water are usable for a possible crystallization in the SFC based on Θ_{stat} measurements and Ca number calculation.

Figure 7 depicts exemplified the solubilities of Ala from 10 °C to 20 °C, 30 °C, 40 °C, and 50 °C in the ternary phase diagram Ala/water/ethanol at 0.1 MPa. The solubility-reducing effect of ethanol is precisely predicted over the entire temperature range due to the excellent agreement between modeled and experimental solubilities. Modeling was performed based on the parameters from Tables 1–3, which were used for the binary systems in Figure 6. No additional parameters were fitted. Thus, PC-SAFT shows a high capability in predicting solubilities in solvent mixtures at different temperatures. This is valid in the same way for the ternary systems of Arg/water/ethanol, and APAP/water/ethanol as shown in Figures S1 and S2 in the supplementary information.

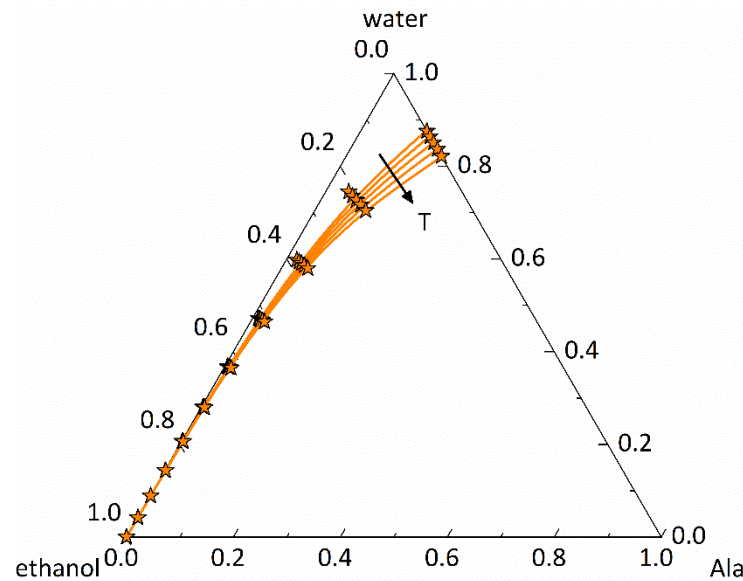


Figure 7. Ternary phase diagram of Ala/water/ethanol at 0.1 MPa with compositions given in mass fractions: Solubility lines were predicted in this work using PC-SAFT, and symbols denote solubility measurements from An et al. [61]. The arrow indicates the direction of increasing temperature from 10 °C to 20 °C, 30 °C, 40 °C, and 50 °C.

In order to obtain the indication about the slug flow stability in the SFC, Table 7 shows the Θ_{stat} measured for different ethanol/water compositions on FEP, as well as the calculated Ca numbers for the respective operating parameters.

From Table 7, it is clear that Θ_{stat} decreases with increasing ethanol fraction. Based on the general definition of non-wetting property for $\Theta > 90^\circ$, the mixtures with w_{EtOH} up to 10 wt.-% are suitable to evoke stable slugs for crystallization inside the SFC. The Ca number increases with higher velocity and rising ethanol content in the mixture.

Figure 8a shows the calculated Ca numbers plotted against the measured Θ_{stat} . The green region marks the previous limits from the literature ($\Theta > 90^\circ$ and $Ca < 10^{-3}$) for a dry pattern. The white regions are the transient regions where data points fulfill only one of the criteria, and, therefore, the slug flow stability at these operating points or for this composition should be experimentally verified. Within the gray region, no stable slug flow should be observable. In our case, only the data points for pure water at volume flow rates of 20 mL min^{-1} and 30 mL min^{-1} are in the green area. None of the mixtures with ethanol content seems to be suitable since they are located in the gray region.

Table 7. Results of Θ_{stat} measurements, observed slug forming mechanism, CAH_{max} , and Ca calculation for different ethanol/water mixtures and velocities in the apparatus. The densities, viscosities, and surface tensions for the mixtures were taken from [79] and used for the calculation of Ca number at $\vartheta = 20^\circ\text{C}$. The Θ_{stat} measurements were conducted at ambient temperature ($\vartheta_{\text{amb}} \approx 22^\circ\text{C}$) and FEP was used as tubing material.

$w_{\text{EtOH}}/\text{wt.-%}$	$\Theta_{\text{stat}}/^\circ$ FEP	Volume Flow Rate/ mL min^{-1}	$Ca/$ -	Flow Pattern Based on Literature Limit ($Ca < 10^{-3}$)	Flow Pattern Based on Experiments	Slug Form Mechanism	$CAH_{\text{max}}/$ -
0	100.66 ± 1.37	20	$5.83 \cdot 10^{-4}$	Dry	Dry	Squeezing	10
		30	$8.74 \cdot 10^{-4}$	Dry	Dry	Squeezing	9
		40	$1.17 \cdot 10^{-3}$	Wet	Dry	Squeezing	9
		60	$1.75 \cdot 10^{-3}$	Wet	Dry	Squeezing	10
10	89.64 ± 4.10	20	$1.18 \cdot 10^{-3}$	Wet	Dry	Squeezing	7
		30	$1.77 \cdot 10^{-3}$	Wet	Dry	Squeezing	11
		40	$2.36 \cdot 10^{-3}$	Wet	Dry	Squeezing	8
		60	$3.55 \cdot 10^{-3}$	Wet	Dry	Transition	11
20	83.39 ± 1.96	20	$2.09 \cdot 10^{-3}$	Wet	Dry	Transition	12
		30	$3.14 \cdot 10^{-3}$	Wet	Dry	Transition	12
		40	$4.19 \cdot 10^{-3}$	Wet	Dry	Transition	9
		60	$6.28 \cdot 10^{-3}$	Wet	Dry	Dripping	16
30	78.65 ± 1.84	20	$3.07 \cdot 10^{-3}$	Wet	Dry	Transition	13
		30	$4.61 \cdot 10^{-3}$	Wet	Dry	Transition	10
		40	$6.15 \cdot 10^{-3}$	Wet	Dry	Dripping	12
		60	$9.22 \cdot 10^{-3}$	Wet	Wet	Dripping	19
50	44.20 ± 2.74	20	$4.25 \cdot 10^{-3}$	Wet	Dry	Dripping	13
		30	$6.37 \cdot 10^{-3}$	Wet	Wet	Dripping	21
		40	$8.49 \cdot 10^{-3}$	Wet	Wet	Dripping	19
		60	$1.27 \cdot 10^{-2}$	Wet	Wet	Dripping	17

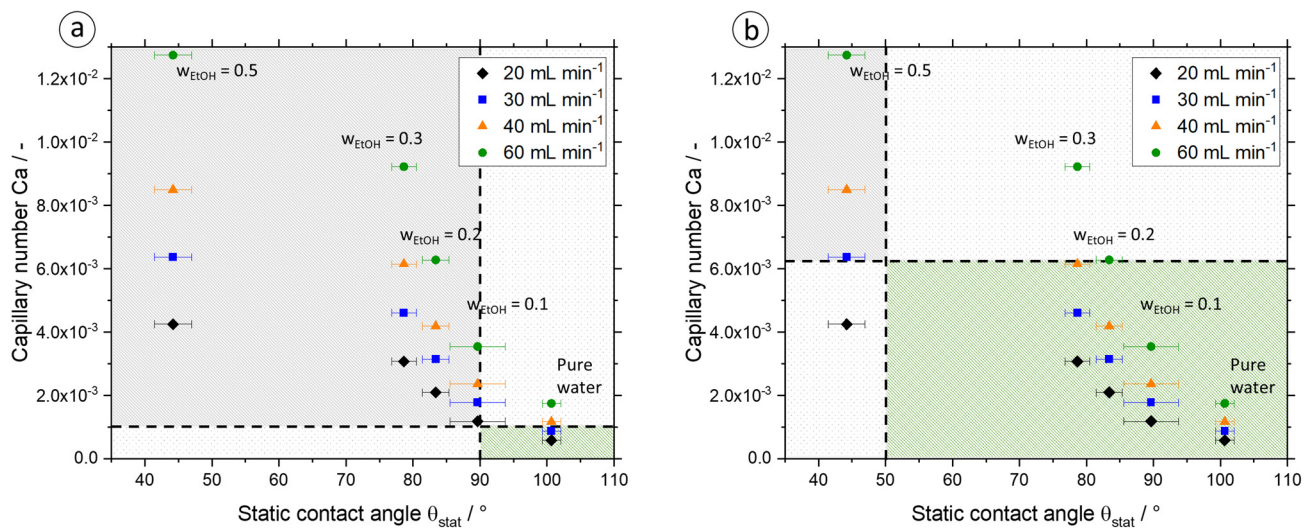


Figure 8. The Ca number is plotted against the Θ_{stat} for different EtOH/water compositions and volume flow rates. Delineations for the dry pattern are shown via the black dashed lines based on the literature (a) and based on the observations in this work (b). The green area marks the dry pattern, the white area the transition, and the gray area the wet region. The latter is unsuitable for crystallization in the SFC.

This contradicts the observations from our experiments for stable slug flow. Figure 9 shows exemplarily the slug shape formed in the apparatus at a total volumetric flow rate of $Q_{\text{tot}} = 20 \text{ mL min}^{-1}$ for all tested ethanol/water mixtures from $w_{\text{EtOH}} = 0\text{--}50 \text{ wt.-%}$ (All other pictures are given in the supplementary information Figures S3–S7). According to our results, there is a broader green region where stable slug flow is possible and dry flow pattern is formed, also with solvent mixtures, as this is the case for all mixtures in Figure 9.

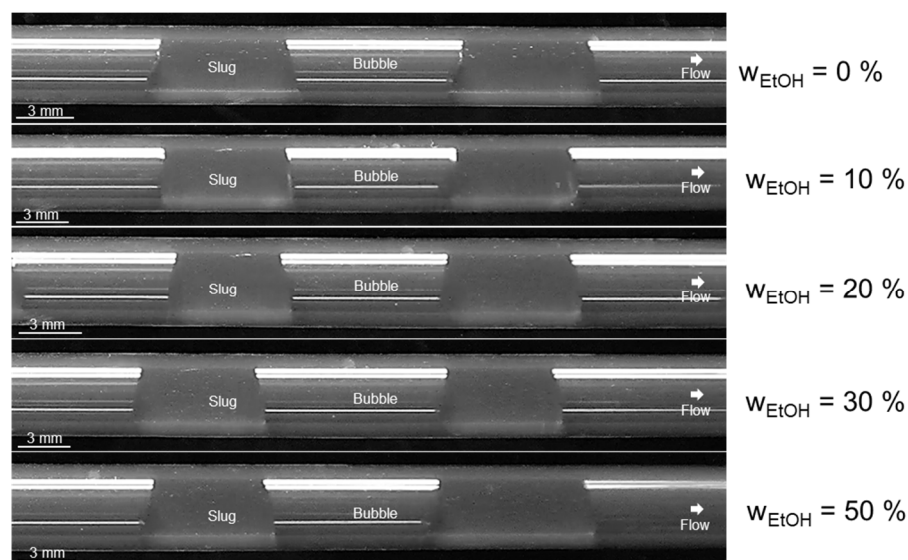


Figure 9. Depiction of the slug flow obtained in the experiments for evaluating the slug shape for different compositions of ethanol/water mixtures at a total volumetric flow rate of $Q_{\text{tot}} = 20 \text{ mL min}^{-1}$ at ambient temperature ($\vartheta_{\text{amb}} \approx 22 \text{ }^{\circ}\text{C}$).

Thus, according to the literature, the suitable region is too small and does not fit to the experimental results. From this, the limits for a stable slug flow for a system and the operating parameters under consideration were modified and given in Figure 8b. The limit of partly wetting region ($\Theta_{\text{stat}} > 50^{\circ}$) can be set as a new limit for the contact angle and $Ca < 6.3 \cdot 10^{-3}$ is set according to the observations. Thus, the range of application is significantly increased, as the majority of the tested mixtures also lie in the stable slug flow area (green area). Operating points or compositions that do not meet any of the criteria should be avoided for crystallization in the SFC.

However, other experimental observations have emerged that should definitely be taken into account for performing reproducible and reliable crystallization in the apparatus. For higher ethanol content, the front interface appears to be more rounded than for lower ethanol content or no ethanol content (experimental observation), confirming the dependence of the meniscus curvature on the Ca number [80].

Furthermore, differences in operation with respect to slug formation could be identified since inside the T-junction a transition state from squeezing to dripping mechanism at the compositions $w_{\text{EtOH}} = 20 \text{ wt.-%}$ and $w_{\text{EtOH}} = 30 \text{ wt.-%}$, and at $w_{\text{EtOH}} = 50 \text{ wt.-%}$ the undesired dripping mechanism was observed. Consequently, the lower interfacial tension of the mixture with rising ethanol content and, correspondingly, the lower contact angle between wall material (T-junction, polypropylene (PP), $\Theta_{\text{PP/wat/air}} = 102^{\circ}$), liquid, and gas lead to a change in the slug formation mechanism. These observations have also been noticed during the handling of higher total volumetric flow rates in the apparatus. The observed slug formation mechanisms and contact angle hysteresis for different compositions and flow velocities are summarized in Table 7. It can be seen that with increasing flow velocity, the transition from squeezing mechanism to dripping mechanism takes place with decreasing ethanol fraction. Accordingly, the operating range in which the SFC is to operate is decisive for the selection of the maximum permissible ethanol content in the

mixture. Consequently, at a volume flow of $Q_{\text{tot}} = 20 \text{ mL min}^{-1}$, an ethanol content of up to $w_{\text{EtOH}} = 10 \text{ wt.-%}$ is permissible in order to enable continuous crystallization operation with high product quality. At a volume flow rate of $Q_{\text{tot}} = 60 \text{ mL min}^{-1}$, on the other hand, an ethanol content should be dispensed with so that a constant slug length and, correspondingly, the same crystallization conditions for each crystal and the condition $\text{RTD}_L = \text{RTD}_S$ can be fulfilled. With regard to the static contact angles in Table 7, this means that contact angles from $\Theta_{\text{stat}} = 80^\circ$ ($w_{\text{EtOH}} = 0.3$) are also theoretically usable in the apparatus, but here, the restriction applies whereby the flow velocity should not be excessively high, since in this case, the slug formation mechanism does not meet the specifications.

6. Conclusions

A quick decision on the suitability of a new solvent system for obtaining a uniform and reproducible product yield with particles of desired size, a narrow width of particle size distribution, and a high purity inside the slug flow crystallizer is possible with the help of an efficient strategy. In this context, particular attention must be paid to slug flow stability and residence time distribution along the tubing, but also to material system-specific criteria for crystallization. In this study, it was shown for several solid components (two amino acids, one API) that selecting a suitable solvent is simplified by using static contact angle measurements and evaluating a dimensionless parameter. Based on the experimental results in this study, the conventional criteria from the literature for the static contact angle (non-wetting behavior for $\Theta_{\text{stat}} > 90^\circ$) or the classification of the flow pattern via the capillary number ($Ca < 10^{-3}$) are not sufficient due to the various relationships in the complex two-phase flow (velocity influence, three-phase interactions, slug formation mechanism, solute influence in the system under consideration, and more). However, by combining the static contact angle and the capillary number, the range of a dry pattern can be reliably estimated. For the system under consideration, three areas can be defined: the dry pattern area, which is limited by $\Theta_{\text{stat}} > 50^\circ$ and $Ca < 6.3 \cdot 10^{-3}$; the transition range, in which only one criterion is reached, and a check for suitability for slug flow stability should be carried out depending on the compositions or the operating conditions; and the range for which no criterion is reached and crystallization in this composition should be avoided in combination with the operating parameters, since a wet pattern results. By using the ranges defined here for Θ_{stat} and Ca number, the possible range of applications for the SFC has been extended.

In addition to these two indicating parameters (Θ_{stat} and Ca), the volatility of the solvent and the solute solubility, and its effect on the contact angle, should also be monitored and backed up by viewing the dynamic contact angle behavior inside the apparatus. Further consideration of the solute's solubility in the solvent via criteria and modeling of the temperature-dependent solubility ensures the prerequisites for successful crystallization in the SFC and reduces the experimental and time effort. However, this is only valid if contamination, and disturbances in the material, for example, can be prevented and uniform operating conditions are maintained. This strategy has been demonstrated for both the binary and ternary systems and, thus, represents a general approach for using different material systems in the apparatus.

Supplementary Materials: The following supporting information can be downloaded at <https://www.mdpi.com/article/10.3390/mi13101795/s1>, Figure S1: Ternary phase diagram of Arg/water/ethanol at 0.1 MPa; Figure S2: Ternary phase diagram of APAP/water/ethanol at 0.1 MPa; Figure S3: Images of water slugs at different flow velocities inside the SFC; Figure S4: Images of ethanol/water slugs ($w_{\text{EtOH}} = 10\%$) at different flow velocities inside the SFC; Figure S5: Images of ethanol/water slugs ($w_{\text{EtOH}} = 20\%$) at different flow velocities inside the SFC; Figure S6: Images of ethanol/water slugs ($w_{\text{EtOH}} = 30\%$) at different flow velocities inside the SFC; Figure S7: Images of ethanol/water slugs ($w_{\text{EtOH}} = 50\%$) at different flow velocities inside the SFC.

Author Contributions: Conceptualization, A.C.K. and K.W.; methodology, A.C.K. and K.W.; software, A.K.; investigation, A.C.K. and A.K.; writing—original draft preparation, A.C.K. and A.K. (equal authorship); writing—review and editing, A.D. and K.W.; visualization, A.C.K. and A.K.; supervision, A.D. and K.W. All authors have read and agreed to the published version of the manuscript.

Funding: This research received no external funding.

Data Availability Statement: All data are contained within the article or the supplementary information.

Acknowledgments: The authors express their special thanks to Daniela Ermeling, Tobias Pape, Marén Schwandt, and Aaron Hiese for the technical support during the experiments.

Conflicts of Interest: The authors declare no conflict of interest. The funders had no role in the design of the study; in the collection, analyses, or interpretation of data; in the writing of the manuscript; or in the decision to publish the results.

Abbreviations

A	Association site
assoc	Association
Ac	Acetone
Ala	L-alanine
amb	Ambient
APAP	Acetaminophen
API	Active pharmaceutical ingredient
Arg	L-arginine
B	Association site
b	Intercept
disp	Dispersion
dyn	Dynamic contact angle
EtOH	Ethanol
FEP	Fluorinated ethylene propylene
hc	Hard chain
i	Component i
IPA	Isopropanol
j	Component j
L	Liquid phase
m	Slope
MSMPR	Mixed-suspension mixed-product removal
PC-SAFT	Perturbed-chain statistical associating fluid theory
PFC	Plug-flow crystallizer
PP	Polypropylene
PSD	Particle size distribution
PVC	Polyvinyl chloride
res	Residual
RTD	Residence time distribution
RTD _L	Residence time distribution of the liquid phase
RTD _S	Residence time distribution of the solid phase
S	Solid phase
SFC	Slug flow crystallizer
stat	Static contact angle
wat	Water

Latin Symbols

a	Helmholtz energy/J mol ⁻¹
c	Concentration/g g ⁻¹
c^*	Saturation concentration/g g ⁻¹
Ca	Capillary number/-
c_p	Heat capacity/J mol ⁻¹
d_h	Hydraulic diameter/mm
d_i	Inner diameter/mm
d_{out}	Outer diameter/mm
$E\delta$	Eötvös number/-
h	Enthalpy/J mol ⁻¹
k	Interaction parameter/-
k_B	Boltzmann constant/J K ⁻¹
L_{50}	Median slug length
L_{90-10}	Width of slug length
L_{tubing}	Length of tubing/m
M	Molar mass/g mol ⁻¹
m^{seg}	Segment number/-
N	Number of sites/-
Q_{air}	Gas volume flow rate/mL min ⁻¹
Q_{liq}	Liquid volume flow rate/mL min ⁻¹
Q_{tot}	Total volume flow rate/mL min ⁻¹
R	Universal gas constant/J mol ⁻¹ K ⁻¹
T	Temperature/K
u	Flow velocity/m s ⁻¹
u	Dispersion energy/J mol ⁻¹
w	Mass fraction/wt.-%
x	Mole fraction/mol mol ⁻¹

Greek Symbols

η	Dynamic viscosity/Pa s
Θ	Three-phase contact angle/°
$\Delta a_{c,SL_{p,i}}$	Slope of linear temperature-dependent heat capacity/J mol ⁻¹ K ⁻²
$\Delta b_{c,SL_{p,i}}$	Intercept of linear temperature-dependent heat capacity/J mol ⁻¹ K ⁻¹
$\sigma_{G/L}$	Gas–liquid interfacial tension/N m ⁻¹
$\sigma_{S/G}$	Solid–gas interfacial tension/N m ⁻¹
$\sigma_{S/L}$	Solid–liquid interfacial tension/N m ⁻¹
θ	Temperature/°C
θ^*	Saturation temperature/°C
γ	Activity coefficient/-
ε	Association energy/J mol ⁻¹
κ	Association volume/-
σ	Segment diameter/Å

References

1. Etminan, A.; Muzychka, Y.S.; Pope, K. Liquid film thickness of two-phase slug flows in capillary microchannels: A review paper. *Can. J. Chem. Eng.* **2021**, *100*, 325–348. [[CrossRef](#)]
2. Kleinebudde, P.; Khinast, J.; Rantanen, J. *Continuous Manufacturing of Pharmaceuticals*; John Wiley & Sons: Hoboken, NJ, USA, 2017.
3. Chen, J.; Sarma, B.; Evans, J.M.B.; Myerson, A.S. Pharmaceutical Crystallization. *Cryst. Growth Des.* **2011**, *11*, 887–895. [[CrossRef](#)]
4. Jiang, M.; Braatz, R.D. Designs of continuous-flow pharmaceutical crystallizers: Developments and practice. *CrystEngComm* **2019**, *21*, 3534–3551. [[CrossRef](#)]
5. Ma, Y.; Wu, S.; Macaringue, E.G.J.; Zhang, T.; Gong, J.; Wang, J. Recent Progress in Continuous Crystallization of Pharmaceutical Products: Precise Preparation and Control. *Org. Process Res. Dev.* **2020**, *24*, 1785–1801. [[CrossRef](#)]
6. Hofmann, G. *Kristallisation in der Industriellen Praxis*; Wiley-VCH: Weinheim, Germany, 2004.

7. Orehek, J.; Teslić, D.; Likozar, B. Continuous Crystallization Processes in Pharmaceutical Manufacturing: A Review. *Org. Process Res. Dev.* **2020**, *25*, 16–42. [[CrossRef](#)]
8. Cote, A.; Erdemir, D.; Girard, K.P.; Green, D.A.; Lovette, M.A.; Sirota, E.; Nere, N.K. Perspectives on the Current State, Challenges, and Opportunities in Pharmaceutical Crystallization Process Development. *Cryst. Growth Des.* **2020**, *20*, 7568–7581. [[CrossRef](#)]
9. Wood, B.; Girard, K.; Polster, C.S.; Croker, D. Progress to Date in the Design and Operation of Continuous Crystallization Processes for Pharmaceutical Applications. *Org. Process Res. Dev.* **2019**, *23*, 122–144. [[CrossRef](#)]
10. Cubaud, T.; Ulmanella, U.; Ho, C.-M. Two-phase flow in microchannels with surface modifications. *Fluid Dyn. Res.* **2006**, *38*, 772–786. [[CrossRef](#)]
11. Etminan, A.; Muzychka, Y.; Pope, K. A Review on the Hydrodynamics of Taylor Flow in Microchannels: Experimental and Computational Studies. *Processes* **2021**, *9*, 870. [[CrossRef](#)]
12. Bretherton, F.P. The motion of long bubbles in tubes. *J. Fluid Mech.* **1961**, *10*, 166. [[CrossRef](#)]
13. Suo, M.; Griffith, P. Two-Phase Flow in Capillary Tubes. *J. Basic Eng.* **1964**, *86*, 576–582. [[CrossRef](#)]
14. Brauner, N.; Maron, D.M. Stability analysis of stratified liquid-liquid flow. *Int. J. Multiph. Flow* **1992**, *18*, 103–121. [[CrossRef](#)]
15. Kandlikar, S.G.; Grande, W.J. Evolution of Microchannel Flow Passages—Thermohydraulic Performance and Fabrication Technology. *Heat Transf. Eng.* **2003**, *24*, 3–17. [[CrossRef](#)]
16. Triplett, K.; Ghiaasiaan, S.; Abdel-Khalik, S.; Sadowski, D. Gas-liquid two-phase flow in microchannels Part I: Two-phase flow patterns. *Int. J. Multiph. Flow* **1999**, *25*, 377–394. [[CrossRef](#)]
17. Chen, L.; Tian, Y.; Karayiannis, T. The effect of tube diameter on vertical two-phase flow regimes in small tubes. *Int. J. Heat Mass Transf.* **2006**, *49*, 4220–4230. [[CrossRef](#)]
18. Shah, M.M. A general correlation for heat transfer during film condensation inside pipes. *Int. J. Heat Mass Transfer* **1979**, *22*, 547–556. [[CrossRef](#)]
19. Termühlen, M.; Etmanski, M.M.; Kryschewski, I.; Kufner, A.C.; Schembecker, G.; Wohlgemuth, K. Continuous slug flow crystallization: Impact of design and operating parameters on product quality. *Chem. Eng. Res. Des.* **2021**, *170*, 290–303. [[CrossRef](#)]
20. Su, M.; Gao, Y. Air-Liquid Segmented Continuous Crystallization Process Optimization of the Flow Field, Growth Rate, and Size Distribution of Crystals. *Ind. Eng. Chem. Res.* **2018**, *57*, 3781–3791. [[CrossRef](#)]
21. Jiang, M.; Braatz, R.D. Low-Cost Noninvasive Real-Time Imaging for Tubular Continuous-Flow Crystallization. *Chem. Eng. Technol.* **2018**, *41*, 143–148. [[CrossRef](#)]
22. Robertson, K.; Flandrin, P.-B.; Klapwijk, A.R.; Wilson, C. Design and Evaluation of a Mesoscale Segmented Flow Reactor (KRAIC). *Cryst. Growth Des.* **2016**, *16*, 4759–4764. [[CrossRef](#)]
23. Scott, C.D.; Labes, R.; Depardieu, M.; Battilocchio, C.; Davidson, M.G.; Ley, S.V.; Wilson, C.C.; Robertson, K. Integrated plug flow synthesis and crystallisation of pyrazinamide. *React. Chem. Eng.* **2018**, *3*, 631–634. [[CrossRef](#)]
24. Levenstein, M.A.; Wayment, L.E.; Scott, C.D.; Lunt, R.A.; Flandrin, P.-B.; Day, S.J.; Tang, C.C.; Wilson, C.C.; Meldrum, F.C.; Kapur, N.; et al. Dynamic Crystallization Pathways of Polymorphic Pharmaceuticals Revealed in Segmented Flow with Inline Powder X-ray Diffraction. *Anal. Chem.* **2020**, *92*, 7754–7761. [[CrossRef](#)] [[PubMed](#)]
25. Pu, S.; Hadinoto, K. Comparative evaluations of bulk seeded protein crystallization in batch versus continuous slug flow crystallizers. *Chem. Eng. Res. Des.* **2021**, *171*, 139–149. [[CrossRef](#)]
26. Pu, S.; Hadinoto, K. Improving the reproducibility of size distribution of protein crystals produced in continuous slug flow crystallizer operated at short residence time. *Chem. Eng. Sci.* **2021**, *230*, 116181. [[CrossRef](#)]
27. Eder, R.J.P.; Schrank, S.; Besenhard, M.O.; Roblegg, E.; Gruber-Woelfler, H.; Khinast, J.G. Continuous Sonocrystallization of Acetylsalicylic Acid (ASA): Control of Crystal Size. *Cryst. Growth Des.* **2012**, *12*, 4733–4738. [[CrossRef](#)]
28. Neugebauer, P.; Khinast, J.G. Continuous Crystallization of Proteins in a Tubular Plug-Flow Crystallizer. *Cryst. Growth Des.* **2015**, *15*, 1089–1095. [[CrossRef](#)]
29. Besenhard, M.O.; Neugebauer, P.; Scheibelhofer, O.; Khinast, J.G. Crystal Engineering in Continuous Plug-Flow Crystallizers. *Cryst. Growth Des.* **2017**, *17*, 6432–6444. [[CrossRef](#)] [[PubMed](#)]
30. Young, T. An essay on the cohesion of fluids. *Philos. Trans. R. Soc. Lond.* **1805**, *95*, 65–87. [[CrossRef](#)]
31. Lee, C.Y.; Lee, S.Y. Pressure drop of two-phase plug flow in round mini-channels: Influence of surface wettability. *Exp. Therm. Fluid Sci.* **2008**, *32*, 1716–1722. [[CrossRef](#)]
32. Barajas, A.; Panton, R. The effects of contact angle on two-phase flow in capillary tubes. *Int. J. Multiph. Flow* **1993**, *19*, 337–346. [[CrossRef](#)]
33. Santos, R.M.; Kawaji, M. DEVELOPMENTS ON WETTING EFFECTS IN MICROFLUIDIC SLUG FLOW. *Chem. Eng. Commun.* **2012**, *199*, 1626–1641. [[CrossRef](#)]
34. Srinivasan, V.; Khandekar, S. Thermo-hydrodynamic transport phenomena in partially wetting liquid plugs moving inside micro-channels. *Sādhanā* **2017**, *42*, 607–624. [[CrossRef](#)]
35. Serizawa, A.; Feng, Z.; Kawara, Z. Two-phase flow in microchannels. *Exp. Therm. Fluid Sci.* **2002**, *26*, 703–714. [[CrossRef](#)]
36. Cubaud, T.; Ho, C.-M. Transport of bubbles in square microchannels. *Phys. Fluids* **2004**, *16*, 4575–4585. [[CrossRef](#)]
37. Thulasidas, T.; Abraham, M.; Cerro, R. Flow patterns in liquid slugs during bubble-train flow inside capillaries. *Chem. Eng. Sci.* **1997**, *52*, 2947–2962. [[CrossRef](#)]
38. Skartsis, L.; Khomami, B.; Kardos, J.L. The effect of capillary pressure on the impregnation of fibrous media. *SAMPE J.* **1992**, *28*, 19–24.

39. Maximino, R.B. Surface tension and density of binary mixtures of monoalcohols, water and acetonitrile: Equation of correlation of the surface tension. *Phys. Chem. Liq.* **2009**, *47*, 475–486. [[CrossRef](#)]
40. Wohlgemuth, K.; Schembecker, G. Modeling induced nucleation processes during batch cooling crystallization: A sequential parameter determination procedure. *Comput. Chem. Eng.* **2013**, *52*, 216–229. [[CrossRef](#)]
41. Vetter, T.; Burcham, C.; Doherty, M.F. Regions of attainable particle sizes in continuous and batch crystallization processes. *Chem. Eng. Sci.* **2014**, *106*, 167–180. [[CrossRef](#)]
42. Grant, D.; Mehdizadeh, M.; Chow, A.-L.; Fairbrother, J. Non-linear van't Hoff solubility-temperature plots and their pharmaceutical interpretation. *Int. J. Pharm.* **1984**, *18*, 25–38. [[CrossRef](#)]
43. Vazquez, G.; Alvarez, E.; Navaza, J.M. Surface Tension of Alcohol Water + Water from 20 to 50 °C. *J. Chem. Eng. Data* **1995**, *40*, 611–614. [[CrossRef](#)]
44. Howard, K.S.; McAllister, R.A. Surface tension of acetone-water solutions up to their normal boiling points. *AIChE J.* **1957**, *3*, 325–329. [[CrossRef](#)]
45. Klein, T.; Yan, S.; Cui, J.; Magee, J.W.; Kroenlein, K.; Rausch, M.H.; Koller, T.M.; Fröba, A.P. Liquid Viscosity and Surface Tension of *n*-Hexane, *n*-Octane, *n*-Decane, and *n*-Hexadecane up to 573 K by Surface Light Scattering. *J. Chem. Eng. Data* **2020**, *64*, 4116–4131. [[CrossRef](#)] [[PubMed](#)]
46. Schreiber, M.; Brunert, M.; Schembecker, G. Extraction on a Robotic Platform—Autonomous Solvent Selection under Economic Evaluation Criteria. *Chem. Eng. Technol.* **2021**, *44*, 1578–1584. [[CrossRef](#)]
47. Termühlen, M.; Strakeljahn, B.; Schembecker, G.; Wohlgemuth, K. Characterization of slug formation towards the performance of air-liquid segmented flow. *Chem. Eng. Sci.* **2019**, *207*, 1288–1298. [[CrossRef](#)]
48. Termühlen, M.; Strakeljahn, B.; Schembecker, G.; Wohlgemuth, K. Quantification and evaluation of operating parameters' effect on suspension behavior for slug flow crystallization. *Chem. Eng. Sci.* **2021**, *243*, 116771. [[CrossRef](#)]
49. Prausnitz, J.M. *Molecular Thermodynamics of Fluid-Phase Equilibria*; Prentice-Hall: Englewood Cliffs, NJ, USA, 1969.
50. Do, H.T.; Chua, Y.Z.; Kumar, A.; Pabsch, D.; Hallermann, M.; Zaitsau, D.; Schick, C.; Held, C. Melting properties of amino acids and their solubility in water. *RSC Adv.* **2020**, *10*, 44205–44215. [[CrossRef](#)]
51. Grant, D.J.; Grant, D.J.W.; Higuchi, T. *Solubility Behavior of Organic Compounds*; Wiley: New York, NY, USA, 1990.
52. Chua, Y.Z.; Do, H.T.; Schick, C.; Zaitsau, D.; Held, C. New experimental melting properties as access for predicting amino-acid solubility. *RSC Adv.* **2018**, *8*, 6365–6372. [[CrossRef](#)]
53. Granberg, R.A.; Rasmuson, C. Solubility of Paracetamol in Pure Solvents. *J. Chem. Eng. Data* **1999**, *44*, 1391–1395. [[CrossRef](#)]
54. Neau, S.H.; Bhandarkar, S.V.; Hellmuth, E.W. Differential Molar Heat Capacities to Test Ideal Solubility Estimations. *Pharm. Res.* **1997**, *14*, 601–605. [[CrossRef](#)]
55. Gross, J.; Sadowski, G. Application of the Perturbed-Chain SAFT Equation of State to Associating Systems. *Ind. Eng. Chem. Res.* **2002**, *41*, 5510–5515. [[CrossRef](#)]
56. Held, C.; Cameretti, L.F.; Sadowski, G. Measuring and Modeling Activity Coefficients in Aqueous Amino-Acid Solutions. *Ind. Eng. Chem. Res.* **2011**, *50*, 131–141. [[CrossRef](#)]
57. Ruether, F.; Sadowski, G. Modeling the Solubility of Pharmaceuticals in Pure Solvents and Solvent Mixtures for Drug Process Design. *J. Pharm. Sci.* **2009**, *98*, 4205–4215. [[CrossRef](#)] [[PubMed](#)]
58. Cameretti, L.F.; Sadowski, G. Modeling of aqueous amino acid and polypeptide solutions with PC-SAFT. *Chem. Eng. Process. Process Intensif.* **2008**, *47*, 1018–1025. [[CrossRef](#)]
59. Berthelot, D. Sur le mélange des gaz, Comptes rendus hebdomadaires des séances de l'Académie des. *Sciences* **1898**, *126*, 1703–1855.
60. Lorentz, H.A. Ueber die Anwendung des Satzes vom Virial in der kinetischen Theorie der Gase. *Ann. Phys.* **1881**, *248*, 127–136. [[CrossRef](#)]
61. An, M.; Qiu, J.; Yi, D.; Liu, H.; Hu, S.; Han, J.; Huang, H.; He, H.; Liu, C.; Zhao, Z.; et al. Measurement and Correlation for Solubility of L-Alanine in Pure and Binary Solvents at Temperatures from 283.15 to 323.15 K. *J. Chem. Eng. Data* **2020**, *65*, 549–560. [[CrossRef](#)]
62. Jiménez, J.A.; Martínez, F. Thermodynamic magnitudes of mixing and solvation of acetaminophen in ethanol + water cosolvent mixtures. *Rev. Acad. Colomb. Scienc.* **2006**, *30*, 87–99.
63. Paus, R.; Ji, Y. Modeling and predicting the influence of variable factors on dissolution of crystalline pharmaceuticals. *Chem. Eng. Sci.* **2016**, *145*, 10–20. [[CrossRef](#)]
64. Held, C.; Sadowski, G. *Manual 'ePC-SAFT 1.0'*; TU Dortmund University: Dortmund, Germany, 2017.
65. Wolbach, J.P.; Sandler, S.I. Using Molecular Orbital Calculations to Describe the Phase Behavior of Cross-associating Mixtures. *Ind. Eng. Chem. Res.* **1998**, *37*, 2917–2928. [[CrossRef](#)]
66. Kashid, M.N.; Agar, D.W. Hydrodynamics of liquid-liquid slug flow capillary microreactor: Flow regimes, slug size and pressure drop. *Chem. Eng. J.* **2007**, *131*, 1–13. [[CrossRef](#)]
67. Fu, T.; Ma, Y. Bubble formation and breakup dynamics in microfluidic devices: A review. *Chem. Eng. Sci.* **2015**, *135*, 343–372. [[CrossRef](#)]
68. Fu, T.; Ma, Y.; Funfschilling, D.; Zhu, C.; Li, H.Z. Squeezing-to-dripping transition for bubble formation in a microfluidic T-junction. *Chem. Eng. Sci.* **2010**, *65*, 3739–3748. [[CrossRef](#)]

69. Muzychka, Y.S.; Walsh, E.; Walsh, P. Heat Transfer Enhancement Using Laminar Gas-Liquid Segmented Plug Flows. *J. Heat Transf.* **2011**, *133*, 041902. [[CrossRef](#)]
70. Shao, N.; Gavriilidis, A.; Angeli, P. Effect of Inlet Conditions on Taylor Bubble Length in Microchannels. *Heat Transf. Eng.* **2011**, *32*, 1117–1125. [[CrossRef](#)]
71. Qian, D.; Lawal, A. Numerical study on gas and liquid slugs for Taylor flow in a T-junction microchannel. *Chem. Eng. Sci.* **2006**, *61*, 7609–7625. [[CrossRef](#)]
72. Zhu, C.; Gao, Y.; Li, H.; Meng, S.; Li, L.; Francisco, J.S.; Zeng, X.C. Characterizing hydrophobicity of amino acid side chains in a protein environment via measuring contact angle of a water nanodroplet on planar peptide network. *Proc. Natl. Acad. Sci. USA* **2016**, *113*, 12946–12951. [[CrossRef](#)]
73. Atta, D.Y.; Negash, B.M.; Yekeen, N.; Habte, A.D.; Malik, A.B.A. Influence of natural L-amino acids on the interfacial tension of an oil-water system and rock wettability alterations. *J. Pet. Sci. Eng.* **2020**, *199*, 108241. [[CrossRef](#)]
74. Daldrup, J.-B.G.; Held, C.; Ruether, F.; Schembecker, G.; Sadowski, G. Measurement and Modeling Solubility of Aqueous Multisolute Amino-Acid Solutions. *Ind. Eng. Chem. Res.* **2010**, *49*, 1395–1401. [[CrossRef](#)]
75. Amend, J.P.; Helgeson, H.C. Solubilities of the common L- α -amino acids as a function of temperature and solution pH. *Pure Appl. Chem.* **1997**, *69*, 935–942. [[CrossRef](#)]
76. Granberg, R.A.; Rasmuson, C. Solubility of Paracetamol in Binary and Ternary Mixtures of Water + Acetone + Toluene. *J. Chem. Eng. Data* **2000**, *45*, 478–483. [[CrossRef](#)]
77. Matsuda, H.; Mori, K.; Tomioka, M.; Kariyasu, N.; Fukami, T.; Kurihara, K.; Tochigi, K.; Tomono, K. Determination and prediction of solubilities of active pharmaceutical ingredients in selected organic solvents. *Fluid Phase Equilibria* **2015**, *406*, 116–123. [[CrossRef](#)]
78. Terdenge, L.-M.; Wohlgemuth, K. Impact of agglomeration on crystalline product quality within the crystallization process chain. *Cryst. Res. Technol.* **2016**, *51*, 513–523. [[CrossRef](#)]
79. Khattab, I.S.; Bandarkar, F.; Fakhree, M.A.A.; Jouyban, A. Density, viscosity, and surface tension of water+ethanol mixtures from 293 to 323K. *Korean J. Chem. Eng.* **2012**, *29*, 812–817. [[CrossRef](#)]
80. Giavedoni, M.D.; Saita, F.A. The rear meniscus of a long bubble steadily displacing a Newtonian liquid in a capillary tube. *Phys. Fluids* **1999**, *11*, 786–794. [[CrossRef](#)]